SUBCONTRACT TITLE: IDENTIFYING THE ELECTRONIC PROPERTIES RELEVANT TO IMPROVING THE PERFORMANCE OF HIGH BAND-GAP COPPER BASED I-III-$V1_2$ CHALCOPYRITE THIN FILM PHOTOVOLTAIC DEVICES

SUBCONTRACT NO: XAT-4-33624-08

QUARTERLY TECHNICAL STATUS REPORT FOR: Phase I/Quarter 2
27 July 2004 to 26 October 2004

SUBMITTED TO: Martha Symko-Davies
National Renewable Energy Laboratory

PRINCIPAL INVESTIGATOR: J. David Cohen, Department of Physics
University of Oregon, Eugene, OR 97403
2nd Tier Subcontractor : Jennifer T. Heath, Department of Physic
Linfield College, McMinnville, OR 97128

This report covers the second quarter of Phase I for the period July 27, 2004 to October 26, 2004, of the Phase IB High Performance PV Subcontract XAT-4-33624-08. The work we carried out during this period is primarily related to the evaluation of the electronic properties of the $Cu(InGa)(SeS)_2$ alloys (Task 1), with some additional work related to the evaluation of properties of the CIAS alloys (Task 3). We have also expanded upon our analysis of the high frequency admittance methods (Task 4) that we reported upon in our previous Quarterly Report.

In early August we received the first in an anticipated series of higher bandgap $Cu(InGa)(SeS)_2$ alloy samples from Bill Shafarman at IEC. This first sample device incorporated the endpoint $CuInS_2$ absorber (Sample #24138.32). It was deposited on Mo coated soda lime glass with a Cu-rich composition which resulted in a Cu_xS_y layer on the surface. This was etched off, and then the device was completed with CdS, ZnO and ITO layers. The resulting cell performance was characterized at IEC. Because some hysterisis was exhibited in the IV curves, the efficiency was given as lying between 6.8 to 7.6%, with J_{SC} = 19.39 mA/cm^2, V_{OC} lying between 0.618 and 0.638 volts, and fill factors lying between 0.569 and 0.612. The bandgap of $CuInS_2$ is 1.53eV.

To begin to characterize the electronic properties of these samples we employed drive-level capacitance profiling (DLCP) to establish the carrier densities, high frequency admittance measurements to estimate hole mobilities, and transient photocapacitance (TPC) sub-band-gap spectroscopy to obtain the spectra of defect related optical transitions. Standard (low frequency) admittance measurements were also performed over a range of temperatures, and these results are shown in Fig. 1.

In this frequency range (1kHz-100kHz) very little structure is evident, implying only a small contribution from any deep acceptor states. On the other hand, the junction capacitance is relatively high (over 400pF for this 0.01cm^2 area sample), indicating either a large free carrier density, or perhaps a large deep defect density near the barrier interface.

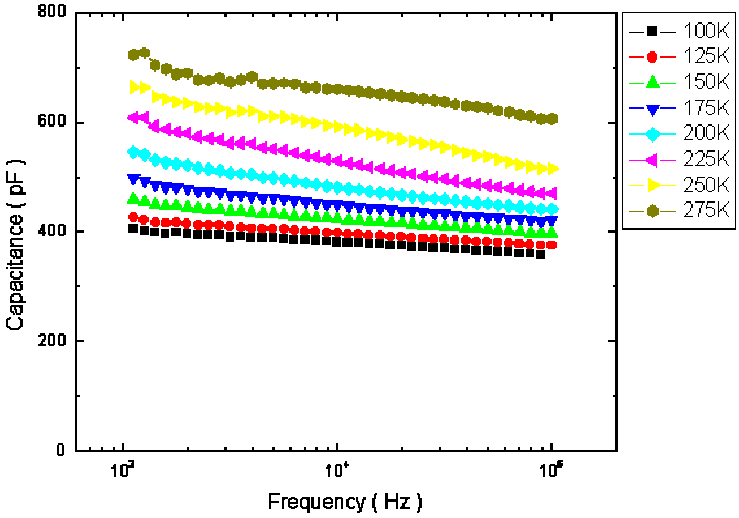

FIG. 1. Low frequency admittance spectra of the $CuInS_2$ sample device acquired at 0V applied bias. These data indicate a relative high carrier density and perhaps some evidence of a deep acceptor level of low density corresponding to the broad admittance step apparent in the higher temperature curves.

In Figure 2 we display 3.3kHz DLCP and CV profiling data at two measurement temperatures. Here we observe a nearly temperature independent DLCP density of 4-5 × 10^{16}cm^{-3}. Increasing the frequency to 80kHz while decreasing the temperature to 200K was not found to affect these values appreciably. On the other hand, the standard CV profiles appear to be roughly 2 × 10^{16}cm^{-3} higher than the DLCP values. This suggests the presence of deeper acceptors; however, because they do not appear as part of the DLCP response, these states must lie at least 0.4eV above E_V.

Figure 3 displays one admittance spectrum obtained using our high frequency bridge. Unlike the high frequency admittance data reported last quarter for CIGS samples, the dielectric freeze-out occurs at a significant lower frequency. If the DLCP densities actually reflect free hole carrier densities in this $CuInS_2$ sample, then this dielectric freeze-out behavior would imply a hole mobility below 1cm^2/Vs. However, additional measurements will be needed to verify that the DLCP densities reflect the true free hole densities in these samples.

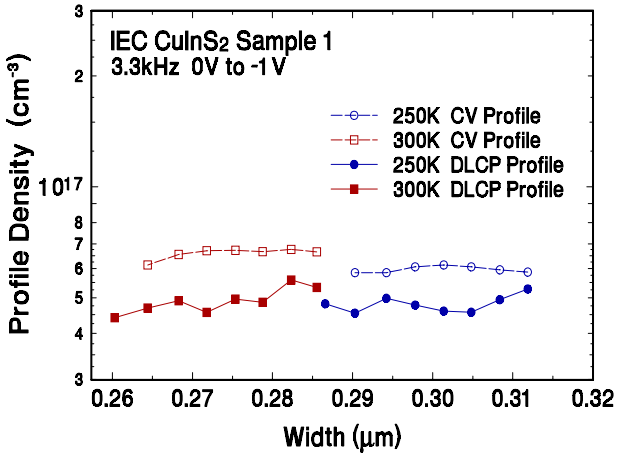

FIG. 2. 3.3kHz DLCP and standard CV profiles at two temperatures. The DLCP densities are nearly independent of temperature and may reflect hole carrier densities.

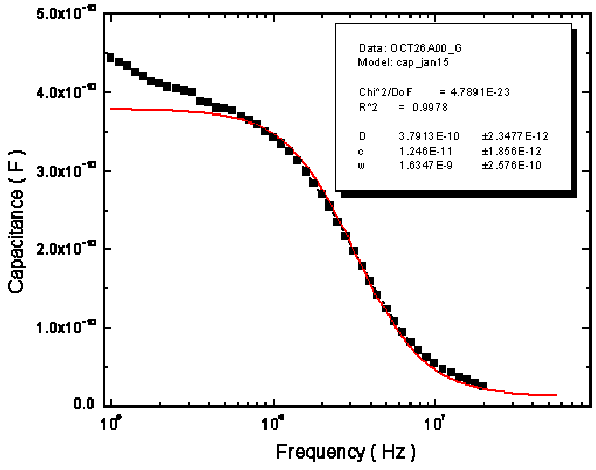

FIG. 3. High frequency admittance spectrum obtained at 125K and 0V applied bias. The fitted solid line indicates a dielectric freeze-out value of ρε near 1.6ns.

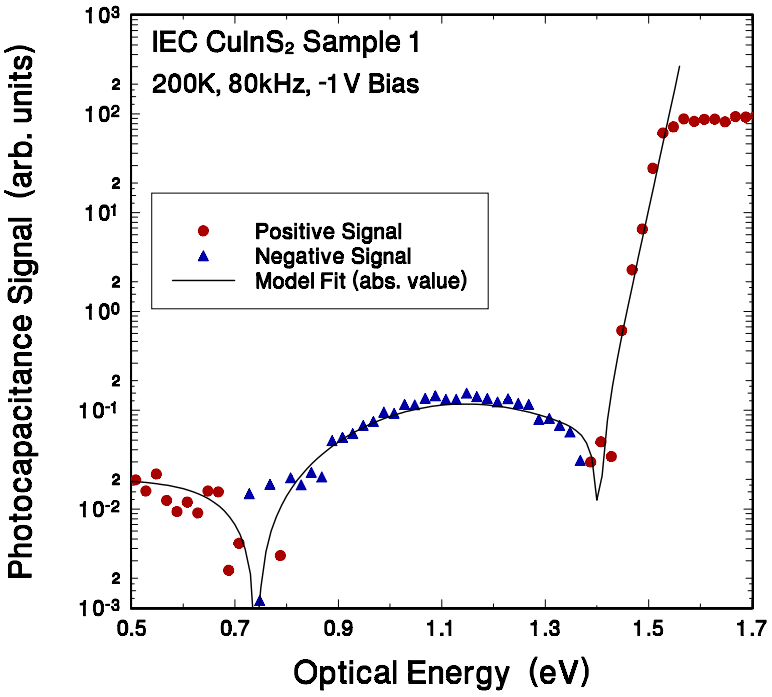

FIG. 4. Transient photocapacitance spectrum for the $CuInS_2$ sample device recorded at 200K and 80kHz using an ambient reverse bias of -1V with voltage filling pulses to 0V. Note that the TPC signal is *positive* at the lowest and highest optical energies (the red circles) which indicates that the optical excitation induces holes to predominantly leave the depletion region, while the TPC signal is *negative* between 0.8 and 1.4eV (the blue triangles), which indicates that more electrons are leaving. This latter case suggests that the photons are predominantly exciting electrons from filled defect levels into the conduction band. The thin solid line is a fit to the data using a preliminary density of states model. An Urbach energy of 18meV is found to fit the bandtail region extending between 1.4 and 1.5eV.

Figure 4 displays one transient photocapacitance (TPC) spectrum obtained for the $CuInS_2$ sample device. This spectrum is unusual compared to all of the previous TPC spectra we have obtained for chalcopyrite sample devices in that it exhibits a region of *negative* photocapacitance signal between 0.8 and 1.4eV. This indicates a band of optical induced transitions between an occupied defect band in the depletion region to the conduction band. This then leads to a net loss of negative charge from the depletion region. In contrast, at optical energies below 0.7eV, the predominant optical transition appears to be between the valence band and an empty defect band in the gap, leading to a net loss of holes. Although a preliminary density of states model appears to fit this TPC spectrum very well (the thin solid line in Fig. 4), a complete analysis awaits our collection of TPC spectra over a wider range of measurement temperatures, as well as measurements using the transient junction photocurrent method. One obvious interesting question concerns the effect of the defect band responsible for the negative photocapacitance spectra on the solar cell device performance. We will hopefully be able to address this question when additional CIGSS devices become available for study.

Next we turn to our work under Task 3: Evaluating the $Cu(InAl)Se_2$ alloys. We had previously received a series of four samples from IEC and had characterized these samples using DLCP and photocapacitance spectroscopy. Figure 5 reproduces the set of TPC spectra we had obtained for this series of samples. This set of data clearly illustrates a key puzzling aspect of the CIAS alloys; namely, that while the 13at.% Al alloy the spectrum appears nearly identical to those of $Cu(InGa)Se_2$ alloys with the same bandgap, the CIAS alloys with Al fractions of 29at.% or higher exhibit much broader bandtails with Urbach energies of 27, 42, and 35meV for the alloys with Al fractions of 29, 35, and 48at.%, respectively. These higher Urbach energies are likely to lead to poorer minority carrier mobilites and thus may partially account for the poorer solar cell performance that is observed for these higher Al alloy devices.

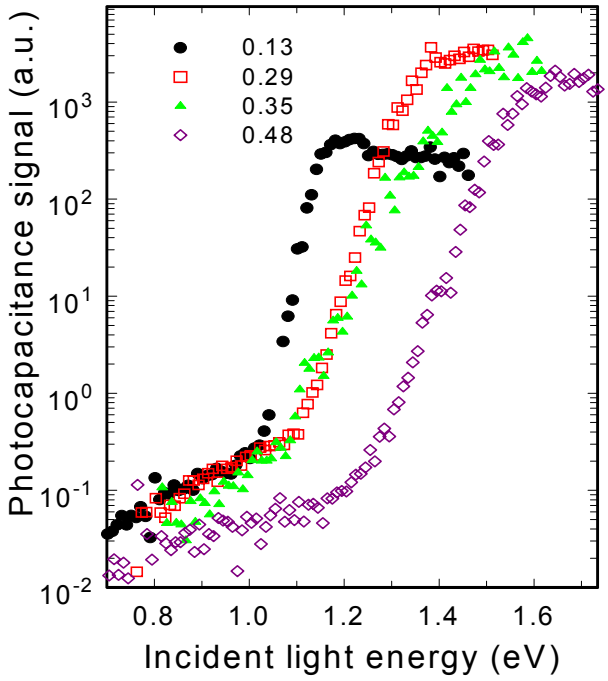

FIG. 5. Transient photocapacitance spectra for four Cu(InAl)Se_2 alloy samples with the Al fractions indicated. Much broader bandtails are exhibited for the 3 higher Al alloy samples. The 35at.% Al sample exhibits an anomalous higher degree of bandtail broadening.

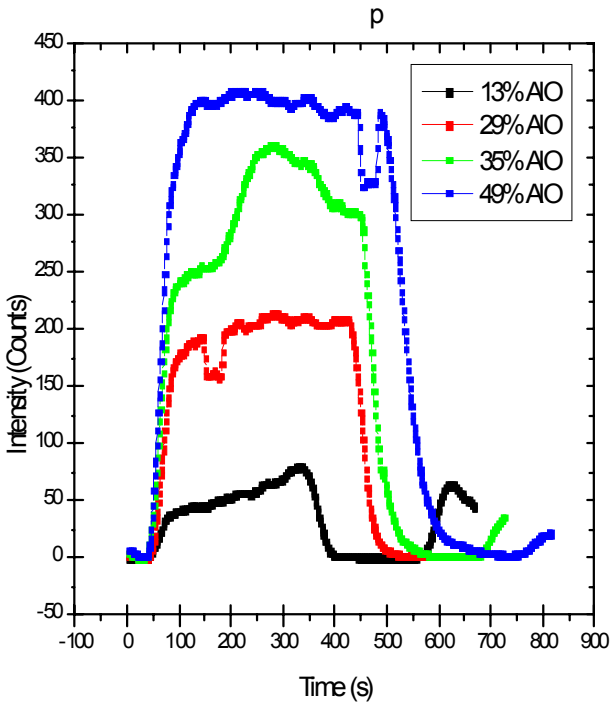

FIG. 6. SIMS compositional profiles of the Al content for the four Cu(InAl)Se_2samples. Note the large spatial variation in the 35at.% Al sample which helps explain the anomalous bandtail broadening seen in the TPC spectrum of this sample.

This result from our photocapacitance measurements came as a bit of a surprise because the higher Ga CIGS alloys did not exhibit significantly larger values of Urbach energy compared to the lower Ga samples. Moreover, in comparing the TPC spectra for the 29, 35, and 48at.% Al alloys in Fig. 5 we see that the 35at.% sample actually exhibits a substantially broader and somewhat less exponential bandtail than the other two high Al samples. During the past summer the Materials Science Institute at my University acquired a TOF-SIMS instrument. Thus, we decided to analyze the set of CIAS samples to find out whether compositional disorder in these samples might account for the higher Urbach energies that are exhibited.

In Fig. 6 the results of this SIMS analysis is shown for the Al fraction of these 4 sample devices. Here we see very uniform compositions for the 29at.% and 48at.% sample, but not so uniform for the other 2 samples. Actually, if one looks at the Al profiles in comparison to the In profiles, the nonuniformity in the 13at.% sample is much smaller; however, the anomaly for the 35at.% persists. That is, the 35at.% sample is found to be the only sample with significant variations in the Al/In ratio. This, undoubtedly, is the reason that the sub-band-gap optical spectrum indicated a greater degree of disorder for this sample. On the other hand, the generally broader bandtails for the other higher Al alloys cannot be simply explained by compositional inhomogeneities, at least not on the length scale accessible to SIMS profiling. Thus, the reason for the general deterioration of the electronic properties of these higher Al alloys remains a mystery.

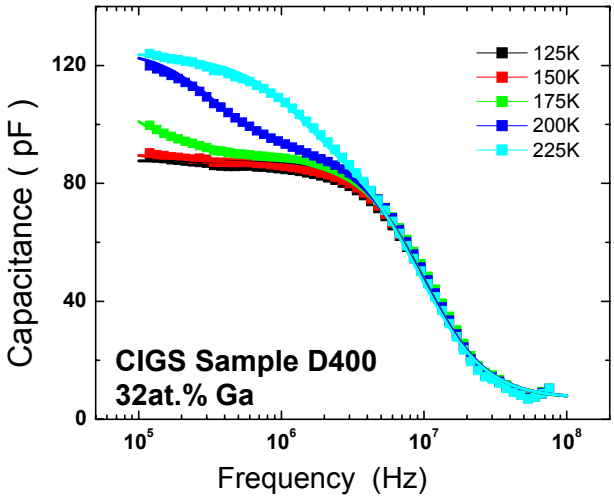

FIG. 7(a). Capacitance vs. frequency spectra at high frequencies for one CIGS sample at –1V bias. The data at each temperature have been fitted using the SCAPS modeling program with the parameters given in Table I. Because the fits are so good, these lines mostly obscured.

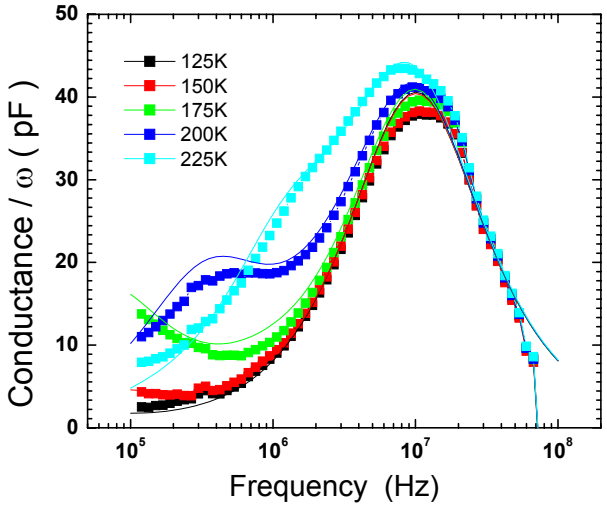

FIG. 7(b). Conductance/w vs. frequency spectra at high frequencies that represents the real part of the admittance data shown in Fig. 7(a). The thin solid lines from the SCAPS model fit are also shown.

The final area of effort we wish to report for this period is related to Task 4, and represents a continuation of the work reported for the 1st Quarter of this Subcontract. This pertains to our implementation of high frequency admittance measurements to better understand majority carrier transport properties in the chalcopyrite materials. In our 1st Quarterly report we concluded that both the resistivities and hole carrier densities in the CIGS samples we had measured had at most a very weak temperature dependence. This implied a nearly temperature independent mobility in the temperature range 100K to 175K. However, at higher temperatures our simple network analysis was insufficient because the deep acceptors could also respond in the same high frequency regime that was undergoing the dielectric freeze-out. This led to more complex admittance behavior involving both the carrier dynamics and the deep state response. An example of the types of complex admittance behavior that is observed is shown in Fig. 7.

Although my laboratory has available a fairly extensive admittance numerical modeling capability, our own analysis does not take into account effects that arise when carrier transport is slow compared to the characteristic times of the applied frequencies. However, the SCAPS program developed by Marc Burgelman's group at the University of Gent includes this in their ac response analysis. Thus, we decided to apply this analysis to some of the high frequency admittance data we had collected on the CIGS alloy samples.

TABLE I. SCAPS Model Parameters used to obtain fits to high frequency admittance spectra displayed in Figure 7.

Hole Mobility μ_h cm^2/Vs	Hole Carrier Density (cm^{-3})	Defect Density (cm^{-3})	Defect Energy eV above E_V	Emission Prefactor, ν (sec^{-1})
7.0	6×10^{14}	2.4×10^{15}	0.185	5.5×10^{10}

Initially results were poor due to apparent problems with the numerics when we assumed a Gaussian distribution for the deep acceptor energy distribution. However, these types of problems disappeared when we assigned the deep acceptor a single discrete energy. Since the deep acceptor in these samples has quite a narrow energy distribution in any case, approximating it with a single discrete energy still allowed us to obtain quite good fits to the admittance data. These fits are indicated by the thin lines in Fig. 7. We believe that the small remaining discrepancies could be eliminated if the program allowed us to accurately calculate with narrow Gaussian distributions.

The parameters used to obtain the fits shown in Fig. 7 are listed in Table I. Note that the thermal emission prefactor listed for the deep acceptor was taken to be independent of temperature.[1] These fits assumed a constant, temperature independent carrier density and mobility over the entire series of temperatures shown. Therefore, this strengthens our conclusion that the carrier densities and mobility are indeed nearly constant over the temperature regime of our measurements for the set of CIGS samples we have studied.

[1]. If one assumes a T^2 temperature dependence to the thermal emission prefactor, then the activation energy for the deep acceptor should be decreased by about 30meV to 0.155eV.